J. Fluid Mech. (2024), *vol*. 985, A41, doi:10.1017/jfm.2024.309

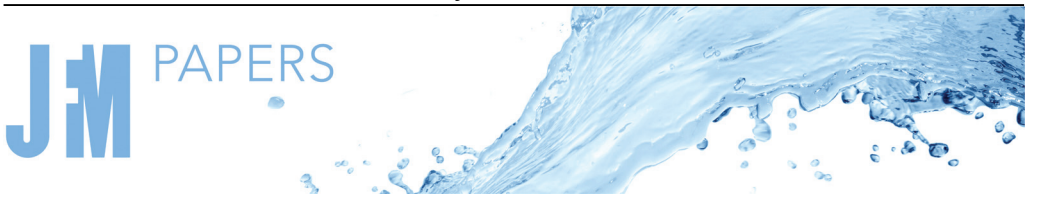

Instability mechanisms initiating laminar–turbulent transition past bioprosthetic aortic valves

Karoline-Marie Bornemann[1],† **and Dominik Obrist**[1]

[1] ARTORG Center for Biomedical Engineering Research, University of Bern, Freiburgstrasse 3, 3010 Bern, Switzerland

(Received 3 October 2023; revised 2 February 2024; accepted 23 March 2024)

Bioprosthetic heart valves create turbulent flow during early systole which might be detrimental to their durability and performance. Complex mechanisms in the unsteady and heterogeneous flow field complicate the isolation of specific instability mechanisms. We use linear stability analysis and numerical simulations of the flow in a simplified model to study mechanisms initiating the laminar–turbulent transition. The analysis of a modified Orr–Sommerfeld equation, which includes a model for fluid–structure interaction (FSI), indicates Kelvin–Helmholtz and FSI instabilities for a physiological Reynolds number regime. Two-dimensional parametrized FSI simulations confirm the growth rates and phase speeds of these instabilities. The eigenmodes associated with the observed leaflet kinematics allow for decoupled leaflet oscillations. A detailed analysis of the temporal evolution of the flow field shows that the starting vortex interacts with the aortic wall leading to a secondary vortex which moves towards the shear layer in the wake of the leaflets. This appears to be connected to the onset of the shear layer instabilities that are followed by the onset of leaflet motion leading to large-scale vortex shedding and eventually to a nonlinear breakdown of the flow. Numerical results further indicate that a narrower aorta leads to an earlier onset of the shear layer instabilities. They also suggest that the growing perturbations of the shear layer instability propagate upstream and may initiate the FSI instabilities on the valve leaflets.

Key words: biomedical flows, blood flow, shear-flow instability

1. Introduction

In aortic valve replacement therapy, moderate to severe aortic stenosis is treated by replacing the diseased native aortic valve by a valve prosthesis which is manufactured

† Email address for correspondence: karoline-marie.bornemann@unibe.ch

either of man-made materials (mechanical heart valve, MHV) or of biological tissue (bioprosthetic heart valve, BHV) (Yoganathan, He & Jones 2004; Head, Çelik & Kappetein 2017). Besides their superior durability, MHVs require life-long anti-coagulation therapy for the patient due to flow-induced thrombogenicity which is caused by excessive shear stresses in the flow field that cause platelet activation (Yun *et al.* 2014; Hedayat, Asgharzadeh & Borazjani 2017; Klusak & Quinlan 2019). A BHV creates a more physiological flow field and exhibits lower thrombogenicity. Nevertheless, turbulent flow during the systolic phase of the cardiac cycle is observed (Becsek, Pietrasanta & Obrist 2020), possibly triggering leaflet calcification and eventually leading to structural valve deterioration (Dvir *et al.* 2018; Gomel, Lee & Grande-Allen 2019; Li 2019; Tsolaki *et al.* 2023) or causing bioprosthetic leaflet thrombosis (Egbe *et al.* 2015; Holmes & Mack 2017; Puri, Auffret & Rodés-Cabau 2017). Therefore, turbulent blood flow after BHVs is detrimental to valve performance and may be a factor for their limited durability of less than 20 years, which prevents their usability for younger patients (Kheradvar *et al.* 2015). To understand the origin of turbulent flow after a BHV, the identification of hydrodynamic instabilities and the understanding of laminar–turbulent transition mechanisms in the vicinity of the valve prosthesis is crucial.

Fluid–structure interaction (FSI) of blood flow and bioprosthetic aortic valves has been described and investigated both experimentally (e.g. Saikrishnan *et al.* 2012; Hasler & Obrist 2018; Jahren *et al.* 2018; Oechtering *et al.* 2019; Lee *et al.* 2020) and numerically (e.g. Borazjani 2013; Bavo *et al.* 2016; de Tullio & Pascazio 2016; Hedayat *et al.* 2017; Chen & Luo 2018; Gilmanov, Stolarski & Sotiropoulos 2018; Becsek *et al.* 2020; Gallo, Morbiducci & de Tullio 2022; Johnson *et al.* 2022; Asadi & Borazjani 2023).

Various complex flow phenomena are present during the opening of the valve. With a central aortic jet emerging from a non-circular time-varying valve orifice area, a highly unsteady downstream flow field is created including a shear layer separating the forward flow towards the ascending aorta (AAo) and the retrograde flow towards three cavities enclosing the valve, known as sinus of Valsalva. Immediately following valve opening, a non-circular starting vortex ring of threefold symmetry is formed which breaks down to smaller-scale vortices shortly thereafter. It marks the onset of turbulence during systolic acceleration (see e.g. figure 5 in Becsek *et al.* (2020)). The identification of hydrodynamic instabilities contributing to this laminar–turbulent transition is intricate due to the existence of various spatial and temporal scales of the flow problem.

Instabilities initiating turbulent flow around MHVs were evaluated by simplification of the problem with a bottom-up approach and a geometrical submodel (Zolfaghari & Obrist 2019; Zolfaghari *et al.* 2022). Highly-resolved two- and three-dimensional direct numerical simulations (DNS) were performed for a rigid, fixed MHV in open systolic position. The use of linear stability analysis (LSA) tools enabled the identification of a pocket of absolute instability which caused nonlinear breakdown of the flow farther downstream. This discovery provided cues for an optimized leaflet design which allowed the delay of the laminar–turbulent transition such that unfavourable flow phenomena downstream of the aortic valve in the AAo could be eliminated.

In contrast to MHVs, bioprosthetic aortic valves include anisotropic, hyperelastic leaflet behaviour which adds to the problem complexity due to FSI (Soares *et al.* 2016). Strongly dependent on the valve design, a complex interplay of downstream turbulence, recirculating flow within the sinus of Valsalva and structural anisotropy of the leaflets may cause so-called fluttering describing a nonlinear oscillating leaflet motion (Lee *et al.* 2021). Previous studies of valve performance in the presence of fluttering have shown

both increased thrombosis risk due to higher turbulent kinetic energy levels (Hatoum *et al.* 2018) and also accelerated valve deterioration due to cyclic stresses (Johnson *et al.* 2020). Therefore, valve fluttering might contribute to the limited long-term durability of BHVs. Experimental as well as computational results have shown the influence of valve diameter and valve thickness on the fluttering frequency (Lee *et al.* 2021). According to results of Johnson *et al.* (2022), reduced flexural stiffness is considered a primary factor for increased leaflet flutter resulting in additional vortex formation in the valve vicinity, blood flow disturbance and an oscillatory pressure field. By varying the leaflet thickness, Chen & Luo (2020) investigated the impact of bending rigidity identifying an optimal range located between reduced rigidity resulting in flapping motion lowering the valve performance index and increased rigidity leading to hampered opening and closing as well as higher resistance. However, whether the origin of laminar–turbulent transition can be linked to hydrodynamic instabilities developing in the downstream flow field or to the active perturbation of the fluid by an oscillating structure remains unclear.

The identification of the mechanisms leading to laminar–turbulent transition past bioprosthetic aortic valves is important to find ways to suppress or control turbulence in the AAo and therefore to prevent unfavourable flow phenomena. Previous computational studies focused on modelling the full kinematic and morphological complexity of a BHV. While this approach leads to comprehensive understanding of large-scale flow phenomena, the interaction of multiple complex flow features like recirculation and shear layers with the fluttering motion of hyperelastic structures complicates the isolation of instabilities with such a top-down approach. Basic fundamental questions remain unanswered such as the specific types of instabilities, their origin and their individual role in the laminar–turbulent transition mechanisms. Thus, we propose a bottom-up approach breaking down the complex flow problem into sub-problems targeting a more isolated and focused study of instability mechanisms.

First, we derive extended Orr–Sommerfeld equations which include FSI to study basic linear instability mechanisms in a simplified one-dimensional model. Second, we perform numerical FSI simulations of simplified two-dimensional models of the aortic root with different geometries (e.g. different aortic diameters) and with rigid or flexible leaflets. The resulting flow fields feature various instabilities which interact in different ways with each other. Finally, a comparison between the results obtained from linear stability analysis and the flow patterns observed in numerical data provides deeper insight into the pathways towards transition.

The remainder of this paper is structured as follows. Section 2 illustrates the developed theoretical framework accounting for FSI in LSA (§ 2.1) and gives an overview of the results of temporal LSA (§ 2.2). Section 3 introduces the governing equations and numerical method of our numerical FSI simulations (§ 3.1) as well as the two-dimensional parametrized aortic model (§ 3.2). Numerical results are described (§ 3.3), specifically focusing on the influence of aortic wall geometry and the relevance of FSI on observed flow phenomena. Section 4 relates results of LSA to the numerical FSI-DNS. Section 5 concludes the paper.

2. Linear stability analysis

2.1. *Derivation of the modified Orr–Sommerfeld equations with FSI extension term*

To first understand the basic instability mechanisms occurring during the interaction of fluid and flexible leaflet tissue, we derive an approach incorporating FSI into the classic Orr–Sommerfeld equations. We conduct temporal LSA for multiple base flows (figure 1)

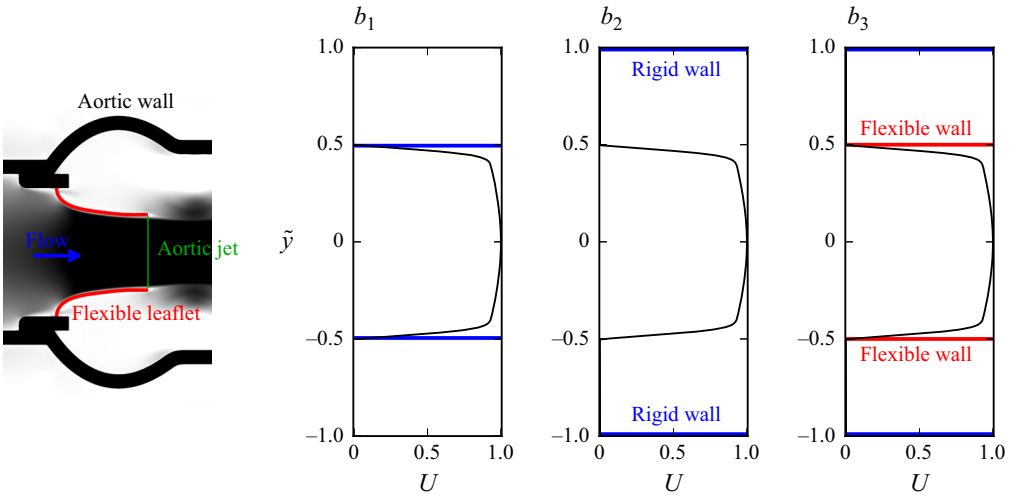

Figure 1. Streamwise velocity field in the aortic root with inserted BHV. Base flow profiles are extracted along the green line (aortic jet) with boundary conditions representing a rigid wall (blue) and flexible wall (red) for the (b_1) wall-bounded case, (b_2) pure shear flow case and (b_3) FSI case with flexible wall.

in a simplified one-dimensional model with and without a flexible wall representing the valve leaflet.

We study three different configurations. Configuration b_1 represents the aortic jet bounded by two fixed leaflets at $\tilde{y} = \pm 0.5$. Configuration b_2 features the same aortic jet after leaving the valve orifice. Two rigid walls represent the aortic walls at $\tilde{y} = \pm 1$ and we assume zero flow between the aortic jet and the rigid walls. In configuration b_3 the aortic jet is bounded by flexible leaflets at $\tilde{y} = \pm 0.5$ which separate the jet from the zero-flow region between the flexible leaflets and the rigid aortic walls at $\tilde{y} = \pm 1$. The definition of the base flow profile for the aortic jet is described in Appendix A. As the applied base flows are slightly asymmetric, we cannot exploit symmetry to retrieve strictly sinous or varicose modes, but need to consider the full domain.

The derivation of the eigenvalue problem starts with the non-dimensional incompressible Navier–Stokes equations (non-dimensional quantities indicated with a tilde) including a force density $\tilde{\boldsymbol{f}}_{FSI}$ which we introduce to account for the interaction between fluid and flexible wall:

$$\frac{\partial \tilde{\boldsymbol{u}}_f}{\partial t} + \rho_f(\tilde{\boldsymbol{u}}_f \cdot \boldsymbol{\nabla})\tilde{\boldsymbol{u}}_f = -\boldsymbol{\nabla}\tilde{p}_f + \frac{1}{Re}\nabla^2\tilde{\boldsymbol{u}}_f + \tilde{\boldsymbol{f}}_{FSI},$$
$$\boldsymbol{\nabla} \cdot \tilde{\boldsymbol{u}}_f = 0. \tag{2.1}$$

The non-dimensionalized force density $\tilde{\boldsymbol{f}}_{FSI}$ depends on a material-specific constant ξ (derivation described in Appendix B) and the second derivative of the wall displacements $\tilde{\eta}_-$ at $\tilde{y} = \tilde{y}_- = -0.5$ and $\tilde{\eta}_+$ at $\tilde{y} = \tilde{y}_+ = 0.5$ to model the effect of wall tension. It is given as

$$\tilde{\boldsymbol{f}}_{FSI} = \left(0, \delta(\tilde{y} - \tilde{y}_-)\xi\frac{\partial^2\tilde{\eta}_-}{\partial\tilde{x}^2} + \delta(\tilde{y} - \tilde{y}_+)\xi\frac{\partial^2\tilde{\eta}_+}{\partial\tilde{x}^2}\right). \tag{2.2}$$

This formulation with the Dirac delta function $\delta(y)$ follows the immersed boundary concept by Peskin (2002). A similar problem with a main focus on flexural stiffness of

the structure has been studied by Lebbal, Alizard & Pier (2022). Here, flexural stiffness (associated with the fourth derivative of the wall displacement) is neglected because of the thin membrane-like geometry of the leaflet.

A normal mode ansatz for the perturbation velocity components $[u', v']$ and perturbation displacements $[\eta'_-, \eta'_+]$ is applied to the linearized extended Navier–Stokes equations:

$$[u', v', \eta'_-, \eta'_+] = [\hat{u}(\tilde{y}), \hat{v}(\tilde{y}), \hat{\eta}_-, \hat{\eta}_+] \exp[\mathrm{i}\alpha(\tilde{x} - c\tilde{t})], \tag{2.3}$$

with associated amplitudes $[\hat{u}(\tilde{y}), \hat{v}(\tilde{y}), \hat{\eta}_-, \hat{\eta}_+]$, wavenumber α and complex phase speed $c = \omega/\alpha$.

The displacement amplitudes $[\hat{\eta}_-, \hat{\eta}_+]$ are substituted by the vertical velocity amplitude $\hat{v}$ considering interface conditions at $\tilde{y} = [\tilde{y}_-, \tilde{y}_+]$:

$$\hat{v}|_{\tilde{y}=\tilde{y}_-} = -\mathrm{i}\alpha c\hat{\eta}_-, \tag{2.4}$$

$$\hat{v}|_{\tilde{y}=\tilde{y}_+} = -\mathrm{i}\alpha c\hat{\eta}_+. \tag{2.5}$$

The insertion of the base flow profile $U = u(x_1, y_1, t)/U_{max}$ leads to a modified Orr–Sommerfeld equation with FSI extension terms:

$$\left[(U-c)(\mathcal{D}^2 - \alpha^2)c - U''c + \frac{\mathrm{i}}{\alpha Re}(\mathcal{D}^2 - \alpha^2)^2 c \right.$$
$$\left. - \alpha^2\delta(\tilde{y} - \tilde{y}_-)\xi - \alpha^2\delta(\tilde{y} - \tilde{y}_+)\xi\right]\hat{v} = 0, \tag{2.6}$$

with $\mathcal{D} = \mathrm{d}/\mathrm{d}\tilde{y}$ and the Reynolds number defined as

$$Re = \frac{U_{max}L\rho_f}{\mu_f}, \tag{2.7}$$

with L as the spanwise orifice of fully open, stable valve leaflets. In this linearized form the positions $y_\pm$ are fixed at ± 0.5.

The resulting quadratic eigenvalue problem

$$(c^2\boldsymbol{A} + c\boldsymbol{B} + \boldsymbol{C})\hat{v} = 0 \tag{2.8}$$

is transformed into a generalized eigenvalue problem (Tisseur 2000)

$$\begin{pmatrix} -\boldsymbol{B} & -\boldsymbol{C} \\ \boldsymbol{I} & \boldsymbol{0} \end{pmatrix}\varphi = c\begin{pmatrix} \boldsymbol{A} & \boldsymbol{0} \\ \boldsymbol{0} & \boldsymbol{I}, \end{pmatrix}\varphi \tag{2.9}$$

with $\varphi = (c\hat{v}, \hat{v})^{\mathrm{T}}$ and the boundary conditions $\hat{v} = \partial\hat{v}/\partial\tilde{y} = 0$ at $\tilde{y} = \pm 1$.

2.2. *Temporal LSA*

First, base flow b_1 with a flow profile between two rigid walls is analysed. It reflects the inflow condition of the aortic jet between two fixed leaflets before entering the AAo. The flow remains linearly stable up to $Re = 5240$.

Beforehand, we define a wavenumber region considered relevant in our later investigation of a finite valve leaflet. Taking into account its one-sided fixation and the finite leaflet length H, we define wavelengths $\lambda_{min} = H$ and $\lambda_{max} = 4H$ as $\alpha_0 = 5.55$ and $\alpha_{1/4} = 1.39$, respectively. As indicated by the schematic drawings in figure 2 and 5 the interval $[\lambda_{min}, \lambda_{max}]$ defines a range of typical wavelengths observed in fluttering valve leaflets (compare, for example, with figure 6 in Becsek *et al.* (2020)).

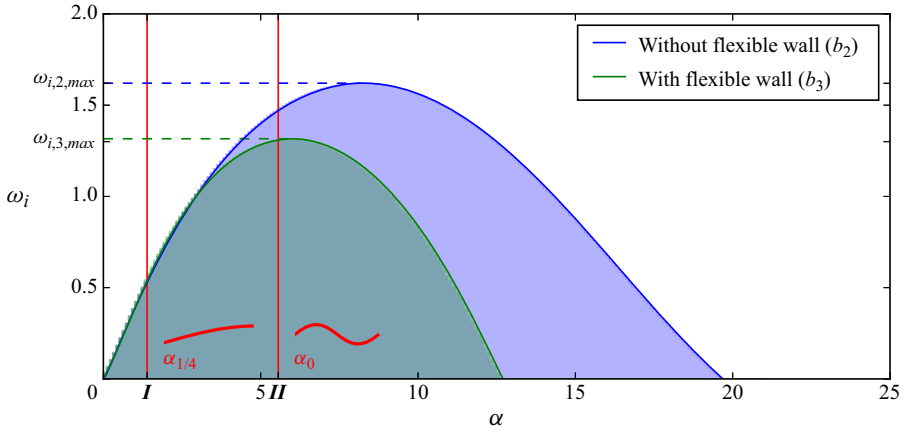

Figure 2. Growth rate ω_i as a function of wavenumber α for $Re = 3318$ for base flow b_2 (blue) and base flow b_3 (green). Eigenfunctions and velocity fields are later given for wavenumbers ***I*** and ***II*** in figures 3 and 4.

The analysis is conducted for base flows b_2 and b_3 to quantify the effect of the flexible wall on stability regions. Growth rates $\omega_i = \mathrm{Im}(c\alpha)$ for a physiologically relevant Reynolds number of $Re = 3318$ (see Appendix A) are shown in figure 2. The separation of zero-flow and jet-flow regions by a flexible wall decreases the range of unstable wavenumbers to $\alpha_3 = [0, 12.7]$ for b_3 compared with the pure shear flow case b_2 which is unstable in $\alpha_2 = [0, 19.7]$. Evaluating the corresponding range of unstable physical wavelengths λ, base flow b_2 shows a minimum unstable wavelength of $\lambda_2 = 0.28H$ while base flow b_3 becomes unstable for a minimum wavelength of $\lambda_3 = 0.44H$. Also, the maximum growth rate of b_3 is smaller and located at a lower wavenumber ($\omega_{i,3,max} = 1.32$ at $\alpha_3 = 6.0$ corresponding to $\lambda_3 = 0.93H$) compared with pure shear flow b_2 ($\omega_{i,2,max} = 1.62$ at $\alpha_2 = 8.2$ corresponding to $\lambda_2 = 0.68H$).

Figure 3 for α_0 and figure 4 for $\alpha_{1/4}$ give further insight into the unstable mode pairs at $Re = 3318$ of base flows b_2 and b_3. Real and imaginary parts of the normalized eigenfunction $\bar{v}$ are shown together with the corresponding reconstructed two-dimensional streamwise velocity fields $\tilde{u}$. The two-dimensional velocity field is reconstructed by

$$\tilde{u}(\tilde{x}, \tilde{y}) = U(\tilde{y}) + \epsilon \mathrm{Re}(\bar{u}(\tilde{y}) \exp[\mathrm{i}\alpha\tilde{x}]), \tag{2.10}$$

$$\tilde{v}(\tilde{x}, \tilde{y}) = \epsilon \mathrm{Re}(\bar{v}(\tilde{y}) \exp[\mathrm{i}\alpha\tilde{x}]), \tag{2.11}$$

with $\bar{u} = \mathrm{i}\mathcal{D}\bar{v}/\alpha$ based on the continuity equation. The wall displacement $[\tilde{\eta}_-(\tilde{x}), \tilde{\eta}_+(\tilde{x})]$ is reconstructed by applying the previously defined interface conditions (2.5):

$$\tilde{\eta}_-(\tilde{x}) = \epsilon \mathrm{Re}\left(\frac{\mathrm{i}}{c\alpha}\bar{v}|_{\tilde{y}_-} \exp[\mathrm{i}\alpha\tilde{x}]\right), \tag{2.12}$$

$$\tilde{\eta}_+(\tilde{x}) = \epsilon \mathrm{Re}\left(\frac{\mathrm{i}}{c\alpha}\bar{v}|_{\tilde{y}_+} \exp[\mathrm{i}\alpha\tilde{x}]\right). \tag{2.13}$$

For α_0 in figure 3, two unstable modes exist for each base flow of which one affects the upper and the other the bottom shear layer (b_2) or flexible wall (b_3). While the real part of the eigenfunction peaks at the distinct vertical location of maximum shear (b_2) or flexible wall (b_3), the location of the imaginary maximum of smaller amplitude is shifted slightly towards the jet core. Considering the reconstructed two-dimensional flow fields, base flow b_2 shows classical Kelvin–Helmholtz (KH) flow features within the shear layer.

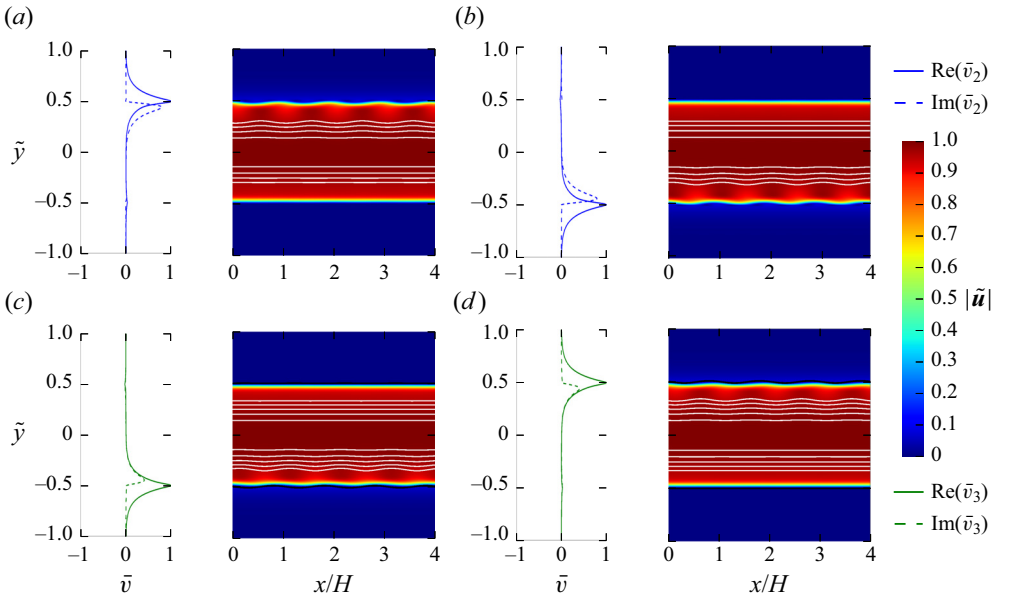

Figure 3. Normalized amplitude $\tilde{v}$ and dimensionless streamwise velocity field $\tilde{u}$ for $\epsilon = 0.08$ with streamlines of (*a*) the most unstable mode of base flow b_2, (*b*) the second most unstable mode of base flow b_2, (*c*) the most unstable mode of base flow b_3 and (*d*) the second most unstable mode of base flow b_3 for wavenumber α_0 at $Re = 3318$ (corresponding to ***II*** in figure 2).

The addition of the flexible wall for base flow b_3 leads to similar flow patterns in the wall region at either $\tilde{y}_-$ or $\tilde{y}_+$. For smaller wavenumbers such as $\alpha_{1/4}$ in figure 4, we can observe an interaction between both shear layers (b_2) or flexible walls (b_3). While higher wavenumbers show a one-sided eigenfunction destabilizing the flow at only one of the vertical locations $\tilde{y}_-$ or $\tilde{y}_+$, lower wavenumbers are associated with eigenfunctions which couple the modes of both shear layers (b_2) or flexible walls (b_3).

When evaluating the neutral stability curves in figure 5, the critical Reynolds number for KH modes corresponding to configuration b_2 is higher ($Re_{KH} = 299$) than for FSI modes corresponding to configuration b_3 ($Re_{FSI} = 184$). An overlapping region of both KH and FSI modes exists for a large Reynolds number and wavenumber range which includes physiologically relevant Reynolds numbers and wavenumbers. Therefore, both instabilities (KH and FSI) are suspected to be present simultaneously after valve opening.

Figure 6 shows the dependency of the eigenvalues on wavenumber α for base flows b_2 and b_3. The growth rate $\omega_i = \mathrm{Im}(c\alpha)$ of the unstable eigenmode pair is displayed against the phase speed $c_r = \omega_r/\alpha$ at $Re = 3318$. In general, the phase speed c_r decreases with increasing wavenumber for both base flow configurations. Growth rates ω_i of KH modes (base flow b_2) peak at higher wavenumber compared with FSI-related modes (base flow b_3). The FSI-related modes generally grow slower than KH modes; however, phase speeds are higher. For $Re = 3318$, the most unstable KH mode has a phase speed $c_r = \omega_r/\alpha$ of $c_{r,2}(\alpha_2) = 0.424$ while the most unstable FSI-related mode is faster with a phase speed of $c_{r,3}(\alpha_3) = 0.649$. In conclusion, unstable KH modes seem to grow faster than unstable FSI-related modes for their unstable wavenumber range. Also, we observe less dependency of the phase speed of the KH modes on the wavenumber. In comparison, FSI-related modes depend stronger on the wavenumber. While small wavelengths travel slowly, the phase speed of higher wavelengths is higher and varies more related to the wavenumber.

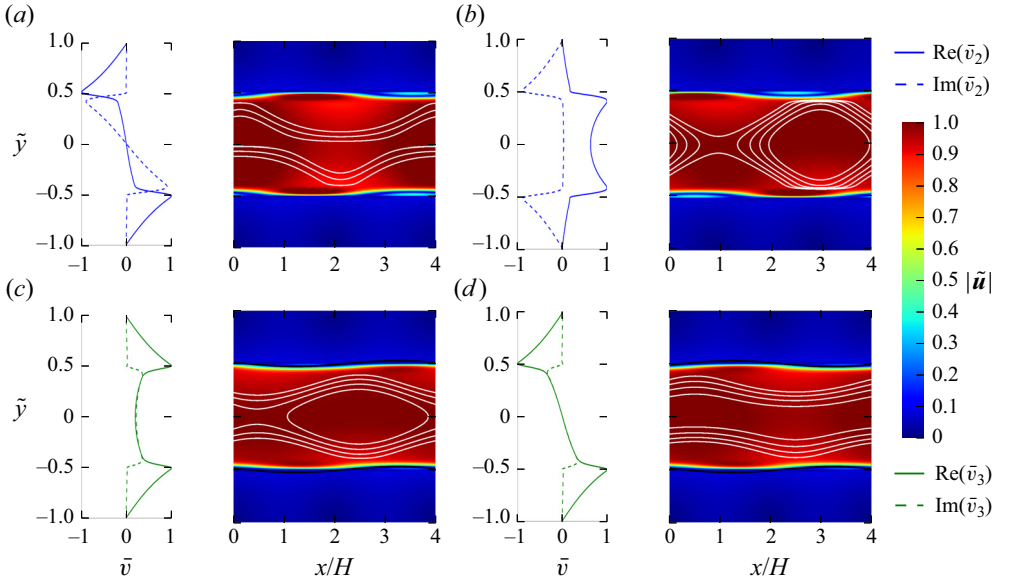

Figure 4. Normalized amplitude $\bar{v}$ and dimensionless streamwise velocity field $\tilde{u}$ for $\epsilon = 0.08$ with streamlines of (*a*) the most unstable mode of base flow b_2, (*b*) the second most unstable mode of base flow b_2, (*c*) the most unstable mode of base flow b_3 and (*d*) the second most unstable mode of base flow b_3 for wavenumber $\alpha_{1/4}$ at $Re = 3318$ (corresponding to ***I*** in figure 2).

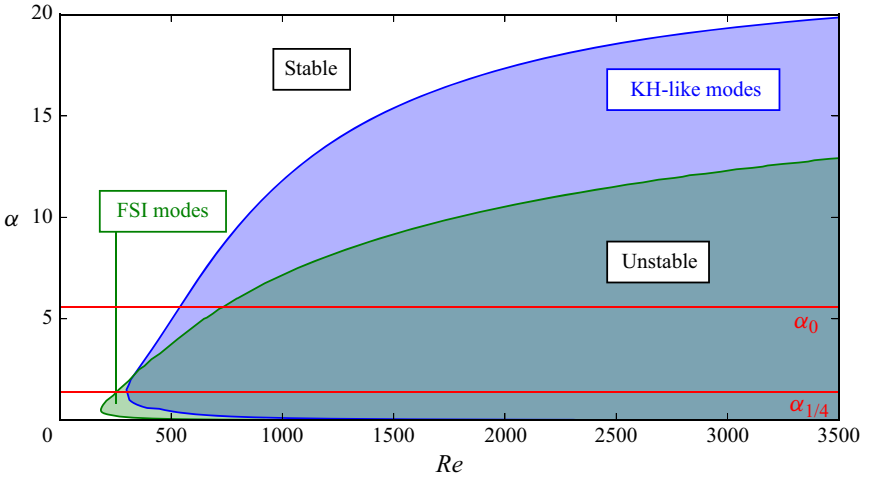

Figure 5. Neutral stability curves for pure shear flow (base flow b_2, indicated in blue) and FSI case (base flow b_3, indicated in green).

3. Numerical FSI simulations

3.1. *Governing equations and numerical method*

After the investigation of instability mechanisms in a simplified one-dimensional model, we now increase the modelling complexity by conducting highly-resolved two-dimensional FSI simulations of a parametrized aortic geometry. Hereby, we aim to obtain a deeper insight into more complex flow features as well as their temporal and spatial evolution.

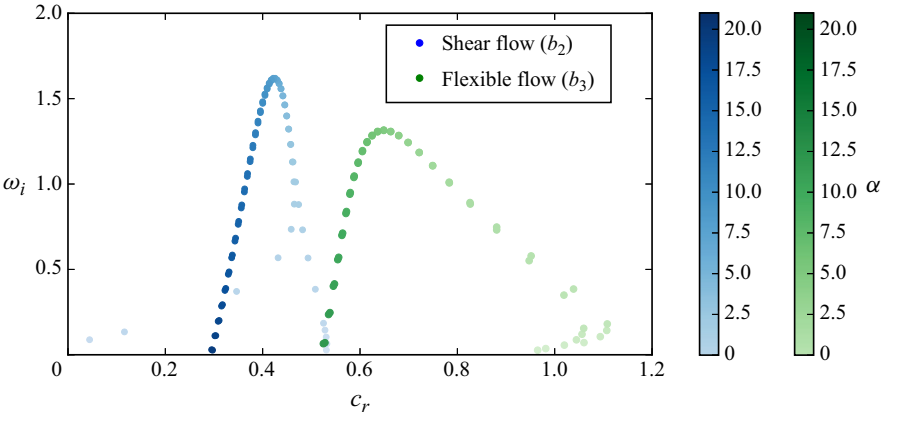

Figure 6. Path of locus for the unstable eigenmode pairs of base flow b_2 (pure shear flow, blue) and base flow b_3 (flexible wall, green) for wavenumbers α at Reynolds number $Re = 3318$.

The interaction of valve and blood flow is implemented within an in-house high-fidelity FSI solver developed for applications including blood flow and soft tissue on hybrid high-performance computing platforms. The flow field is solved by a GPU-accelerated high-order Navier–Stokes solver based on Henniger, Obrist & Kleiser (2010) and Zolfaghari & Obrist (2021) on a structured, staggered grid using the incompressible Navier–Stokes equations:

$$\left.\begin{aligned} \rho_f \frac{\partial \boldsymbol{u}_f}{\partial t} + \rho_f (\boldsymbol{u}_f \cdot \boldsymbol{\nabla}) \boldsymbol{u}_f = -\boldsymbol{\nabla} p_f + \mu_f \Delta \boldsymbol{u}_f + \boldsymbol{f}, \\ \boldsymbol{\nabla} \cdot \boldsymbol{u}_f = 0, \end{aligned}\right\} \tag{3.1}$$

with the fluid density ρ_f, dynamic viscosity μ_f, pressure p_f, time t and, in the present case, two-dimensional fluid velocity field $\boldsymbol{u}_f = [u_{f,x}, u_{f,y}]$. The added force term $\boldsymbol{f}$ accounts for FSI.

Temporal discretization is realized by a third-order Runge–Kutta time stepping while the fluid is spatially discretized by a sixth-order finite difference scheme.

An unstructured grid is used for the discretization of the structural domain, which is solved by a finite element solver using the full elastodynamic equations:

$$\rho_s \frac{\partial^2 \boldsymbol{u}_s}{\partial t^2} - \boldsymbol{\nabla} \cdot \boldsymbol{P} = 0, \tag{3.2}$$

with the structural density ρ_s, the displacement field $\boldsymbol{u}_s$ and the Piola–Kirchhoff stress tensor $\boldsymbol{P}$.

The interaction of fluid and structure motion is realized by a modified immersed boundary method based on variational transfer with the following interface conditions:

$$\left.\begin{aligned} \boldsymbol{u}_f = \frac{\partial \boldsymbol{u}_s}{\partial t}, \\ J^{-1} \boldsymbol{P} \boldsymbol{F}^{\mathrm{T}} \boldsymbol{n} = \boldsymbol{\sigma}_f \boldsymbol{n}, \end{aligned}\right\} \tag{3.3}$$

including the Cauchy stress $\boldsymbol{\sigma}_f$ and the deformation gradient $\boldsymbol{F} = \boldsymbol{\nabla} \boldsymbol{u}_s + \boldsymbol{I}$ with its associated determinant $J = \det \boldsymbol{F}$.

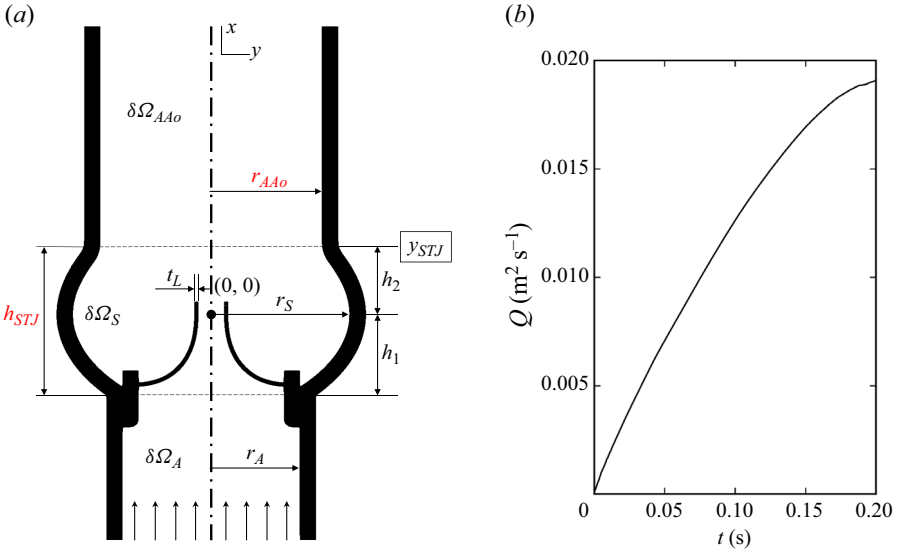

Figure 7. (*a*) Parametrized two-dimensional model of the aortic wall with inserted bioprosthetic valve. Constant parameters (black) are referenced in table 1 and variable parameters (red) in table 2. (*b*) Systolic acceleration defined as the inflow flow rate from the left ventricular outflow tract.

Details of the FSI solver as well as its experimental and numerical validation can be found in Nestola *et al.* (2019) and Becsek *et al.* (2020).

The two-dimensional, rectangular fluid domain is resolved with a structured grid of 2209×897 points on a domain of an extent of $11.18r_A \times 4.55r_A$ with r_A as the annular radius in order to resolve the onset of hydrodynamic instabilities. Grid stretching was applied which reduces the minimal mesh width to around 35 µm in the immediate vicinity of the valve. The unstructured solid grid consists of approximately 11 300 triangular elements.

With a time step size of 1 µs, the computational time for the simulation of the systolic acceleration (200 ms) amounts to around 1500 node hours on 8 nodes of a Cray XC40/XC50 high-performance computer.

3.2. *Two-dimensional parametrized aortic model*

The problem set-up in figure 7(*a*) is a model of an aortic root with an inserted bioprosthetic valve. The actual threefold symmetry of the three-dimensional aortic root with three sinus bulbs and corresponding valve leaflets is simplified to a two-dimensional problem by considering a mirrored longitudinal cut through the middle plane of a leaflet. Generally, the structural domain is divided into aortic wall, valve stent and valve leaflet and separated in the fluid regions as annulus ($\delta\Omega_A$), sinus ($\delta\Omega_S$) and AAo ($\delta\Omega_{AAo}$). The aortic wall geometry is based on data of Haj-Ali *et al.* (2012) and Reul *et al.* (1990) and the curvature of the valve leaflets on the bioprosthetic aortic valve Edwards Intuity Elite 21 (Edwards Lifesciences, Irvine, CA, USA). Geometrical parameters are listed in table 1 which are constant throughout each analysed case.

We additionally introduce the parameters sinus height (h_{STJ}) and AAo radius (r_{AAo}) in order to evaluate the influence of aortic wall geometry on instabilities in the aortic root. Parametrization values (table 2) were chosen according to realistic anatomical ranges

Parameters	Notation	Value
Annular radius	r_A	0.011 m
Sinus radius	r_S	$1.55r_A$
Lower sinus height	h_1	$0.8r_A$
Upper sinus height	h_2	$0.7r_A$
Leaflet thickness	t_L	$0.045r_A$
Location of the sinotubular junction (STJ)	y_{STJ}	$y = h_2$

Table 1. Constant parameters of the parametrized aortic model relative to the annular radius r_A.

Parameter	Initial configuration (A)	Increased sinus height (B)	Decreased AAo radius (C)
h_{STJ}	$1.5r_A$	$1.9r_A$	$1.5r_A$
r_{AAo}	$2.5r_A$	$2.5r_A$	$2.0r_A$

Table 2. Variable parameters of the parametrized aortic model relative to the annular radius r_A with the parameters sinus height h_{STJ} and AAo radius r_{AAo}. Evaluated configurations are indicated as initial configuration (A), increased sinus height (B) and decreased AAo radius (C).

extracted from various studies on aortic root morphology by Bahlmann *et al.* (2011), Buellesfeld *et al.* (2013), Mirea *et al.* (2013), Vriz *et al.* (2014) and Boraita *et al.* (2016). As a result, we define three cases: initial configuration (indicated as case A), increased sinus height (indicated as case B) and decreased AAo radius (indicated as case C).

The opening phase of bioprosthetic aortic valves is completed after a duration of around 20 ms. Thereafter, the valve remains in the open position before the asynchronous closing starts at a third of the full cardiac cycle corresponding to a physical time of about 0.3 s (Vennemann *et al.* 2018). As we aim to investigate hydrodynamic instabilities initiating laminar–turbulent transition leading to turbulent flow during early systole as shown in Becsek *et al.* (2020), we limit our study to the systolic acceleration phase of a duration of about 0.2 s as defined in figure 7(*b*).

Inflow conditions are enforced by the fringe region technique described in Nordström, Nordin & Henningson (1999) for a periodic fluid domain. A penalization term $\boldsymbol{f}_{fringe}(\boldsymbol{x})$ is added to the right-hand side of the Navier–Stokes equations within a fringe region located at the left ventricular outflow tract as described in Becsek *et al.* (2020). A physiological inflow profile at a defined cardiac output is ensured by tuning of the fringe function. By suppressing lateral velocity components within the fringe region, entering fluctuations due to the periodic fluid domain are damped. Here, we impose a pressure difference of 8 mmHg across the fringe region corresponding to the average systolic transvalvular pressure gradient.

The fluid is modelled as incompressible and Newtonian with material properties similar to those of blood ($\mu_f = 0.004$ Pa s, $\rho_f = 1050\,\mathrm{kg\,m^{-3}}$). The aortic wall and the valve stent are assumed to be rigid while we apply a hyperelastic, nonlinear neo-Hookean material model with a shear modulus of $\mu_s = 5.0 \times 10^5$ Pa to the flexible valve leaflets. The shear modulus was tuned in order to match leaflet oscillation amplitudes extracted from a less resolved three-dimensional case of a bioprosthetic valve with leaflets modelled by a fibre-reinforced Holzapfel–Gasser–Ogden model (Holzapfel, Gasser & Ogden 2000). Figure 8 shows the temporal evolution of the leaflet tip displacement for four shear moduli previously applied in studies of Hiromi Spühler & Hoffman (2020) ($\mu_s = 3.3 \times 10^4$ Pa),

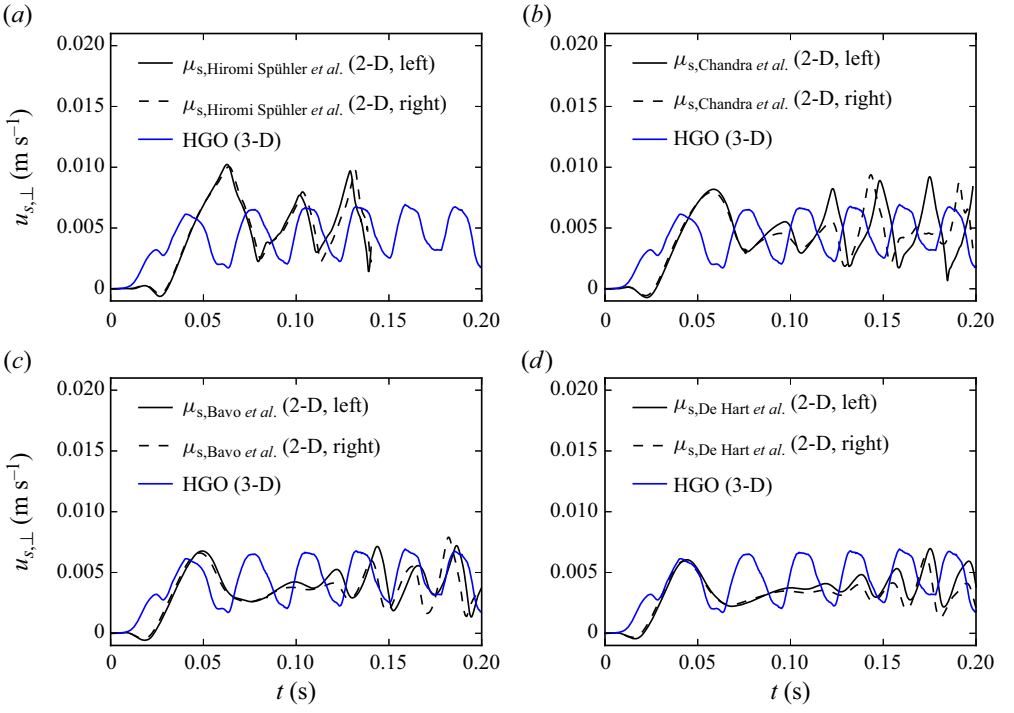

Figure 8. Temporal evolution of leaflet tip displacements perpendicular to the longitudinal aortic axis for four shear moduli according to two-dimensional studies for a neo-Hookean model of (*a*) Hiromi Spühler & Hoffman (2020), (*b*) Chandra, Rajamannan & Sucosky (2012), (*c*) Bavo *et al.* (2016) and (*d*) De Hart *et al.* (2000) in comparison with a less resolved three-dimensional reference study using a Holzapfel–Gasser–Ogden (HGO) model.

Chandra *et al.* (2012) ($\mu_s = 1.2 \times 10^5$ Pa), Bavo *et al.* (2016) ($\mu_s = 3.4 \times 10^5$ Pa) and De Hart *et al.* (2000) ($\mu_s = 5.0 \times 10^5$ Pa) in comparison with the three-dimensional simulation.

3.3. *Numerical results*

3.3.1. *The influence of FSI: rigid versus flexible leaflet*

To assess the effect of FSI on laminar–turbulent transition, we compare the base configuration starting with closed leaflets (case A) from figure 7 with a rigid leaflet case fixed in open position (indicated as AR). The rigid leaflet shape of case AR is extracted from the flexible case A immediately after full valve opening. In particular, we pick the deformed leaflet shape prior to the onset of (*a*) leaflet motion and (*b*) non-zero transversal velocities within the shear layer created in the wake of the leaflet (hereafter referred to as 'leaflet shear layer').

Figure 9 shows the instantaneous viscous shear stress magnitude $|\tau|$ at five time instances for the rigid leaflet case AR (top row) and the flexible leaflet case A (bottom row). Three main flow phenomena seem to occur sequentially for both rigid and flexible cases:

(i) Starting vortex (figure 9*a*). Early during systolic acceleration, a distinct starting vortex is formed which is advected downstream.

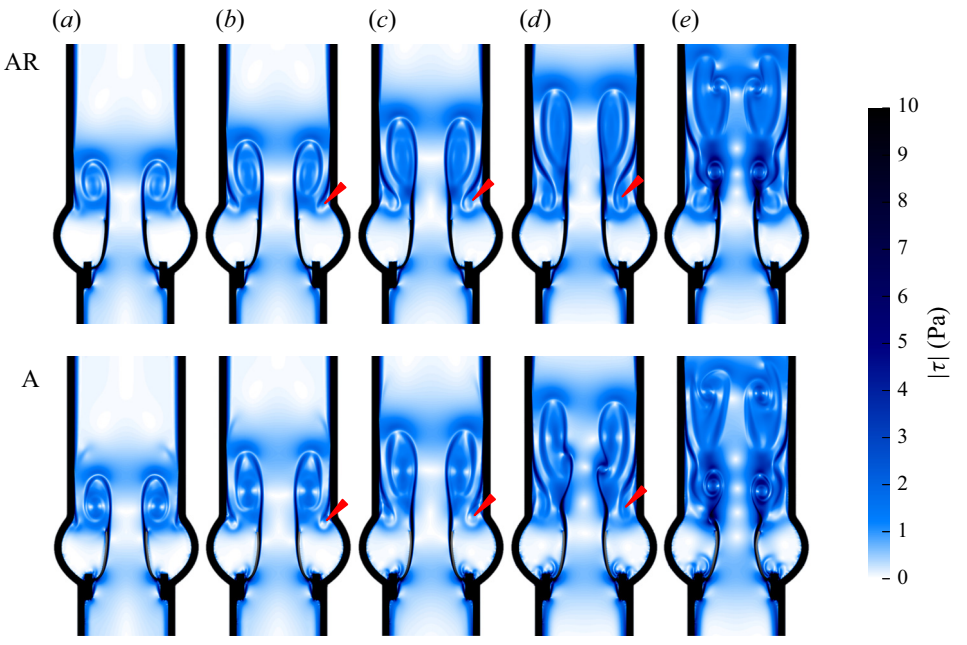

Figure 9. Instantaneous viscous shear stress magnitude $|\tau|$ for (AR) rigid leaflet case and (A) flexible leaflet case for aortic wall configuration A at (*a*) $t = 0.10$ s, (*b*) $t = 0.1175$ s, (*c*) $t = 0.135$ s, (*d*) $t = 0.1525$ s and (*e*) $t = 0.17$ s. Secondary vortical structures forming after the impingement of the starting (primary) vortex on the aortic wall are shown by the red arrows.

(ii) Vortex–wall interaction (figure 9*b–d*). The starting vortex is advected and elongates in the streamwise direction. Due to the transversal confinement by the aortic wall and the associated no-slip boundary condition at the wall, a secondary vortex is created upstream of the starting vortex. This smaller vortex rebounds from the aortic wall and moves towards the leaflet shear layer. The ejection of a secondary vortex when a sufficiently strong primary vortex (here the starting vortex) impinges at a wall is well documented (Walker *et al.* 1987; Orlandi & Verzicco 1993).

(iii) Shear layer instability (figure 9*e*). When the secondary vortex reaches the outer side of the shear layer, we observe growing shear layer instabilities.

Both cases show growing vortical structures within the shear layer at a similar time which suggests that the general mechanisms do not seem to be influenced by the open or closed starting position of the rigid or flexible leaflet, respectively. Moreover, the occurrence of shear layer instabilities seems to be independent of mechanisms related to FSI. This is further supported by the observation that the flexible leaflets of case A remain stable during the initial onset of vortical structures reminiscent of KH-like vortex roll-up within the shear layer. This is in agreement with the LSA predicting KH modes for this flow regime.

The impact of FSI on the downstream flow field starts to become relevant during the growth phase of the shear layer instability. Figure 10 shows instantaneous shear stress magnitudes for the flexible leaflet case at time instances after those displayed in figure 9. As predicted by LSA, we observe an FSI-related instability of the flexible leaflets. While figure 10(*a*) shows the onset of leaflet motion, we observe a stronger influence of leaflet motion on the downstream flow field by vortex shedding from the leaflet tips in figure 10(*b*). This is consistent with the repeated formation of vortex rings at the valve

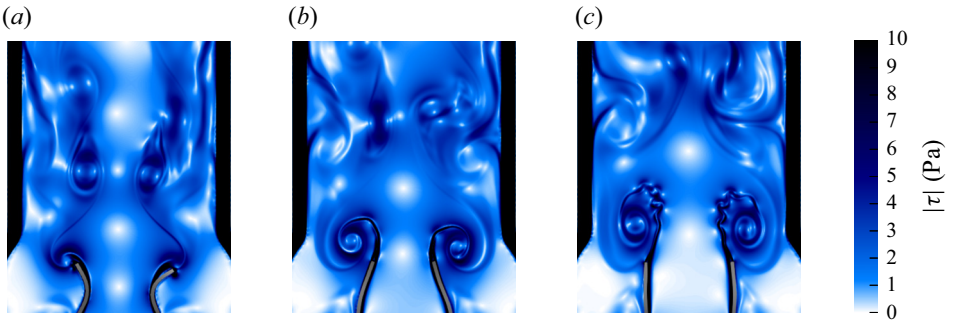

Figure 10. Instantaneous viscous shear stress magnitude $|\tau|$ for aortic wall configuration A at (*a*) $t = 0.1875$ s, (*b*) $t = 0.1945$ s and (*c*) $t = 0.2$ s.

orifice associated with oscillatory leaflet motion shown for the three-dimensional model by Becsek *et al.* (2020). Eventually, figure 10(*c*) possibly indicates another instability leading to small-scale vortices within the larger vortex downstream of the leaflets.

3.3.2. *Effect of aortic root geometry*

To assess the influence of morphological features on instability mechanisms, we simulate the cases A (base configuration), B (increased sinus height) and C (decreased AAo radius) as defined in table 2. Instantaneous viscous shear stress magnitudes at multiple time instances throughout systolic acceleration are shown in figure 11. Cases A and B display similar temporal and spatial evolution of the starting vortex. In contrast, case C exhibits an early elongation of the starting vortex caused by the earlier vortex–wall interaction due to the narrower AAo. As described before, confinement of the downstream flow region causes the formation of a second smaller vortex approaching the leaflet shear layer (red arrows in figure 11) which is followed by instability in the leaflet shear layers. In case C, this shear layer instability appears earlier than in cases A and B (see figure 11*b*). Likewise, the second shear-related instability leading to smaller shear-layer vortices (green arrows) occurs also earlier for case C than for cases A and B.

Figure 12 shows the evolution of the transversal velocity at six leaflet thicknesses, $x = 6t_L$, downstream of the instantaneous leaflet position as well as the transversal leaflet tip velocity. First, we observe the initial opening of the leaflet (completed at $t \approx 0.08$ s) which is almost identical for all three aortic configurations. After the opening phase, the leaflet remains in a stable position until the onset of transversal leaflet and fluid motion. For cases A and B, this occurs at $t \approx 0.13$ s, while we observe an earlier onset of leaflet and fluid motion for case C ($t \approx 0.11$ s). After this onset, we find growing oscillations of leaflet tip and fluid at a frequency of approximately 55 Hz. These oscillations are reminiscent of leaflet fluttering observed in BHVs in experimental studies (Vennemann *et al.* 2018).

Although the same qualitative sequence of flow phenomena shows for every aortic wall configuration, there are major differences in the timing and onset of the different mechanisms. In particular, a shorter distance between leaflet tip and aortic wall appears to lead to earlier shear layer perturbations.

4. Comparison of numerical results and LSA

Finally, we compare the results from LSA (§ 2) with flow patterns observed in numerical simulations (§ 3). Previously, we already confirmed in both approaches the consistent presence of KH and FSI instabilities for the investigated flow regime at $Re = 3318$.

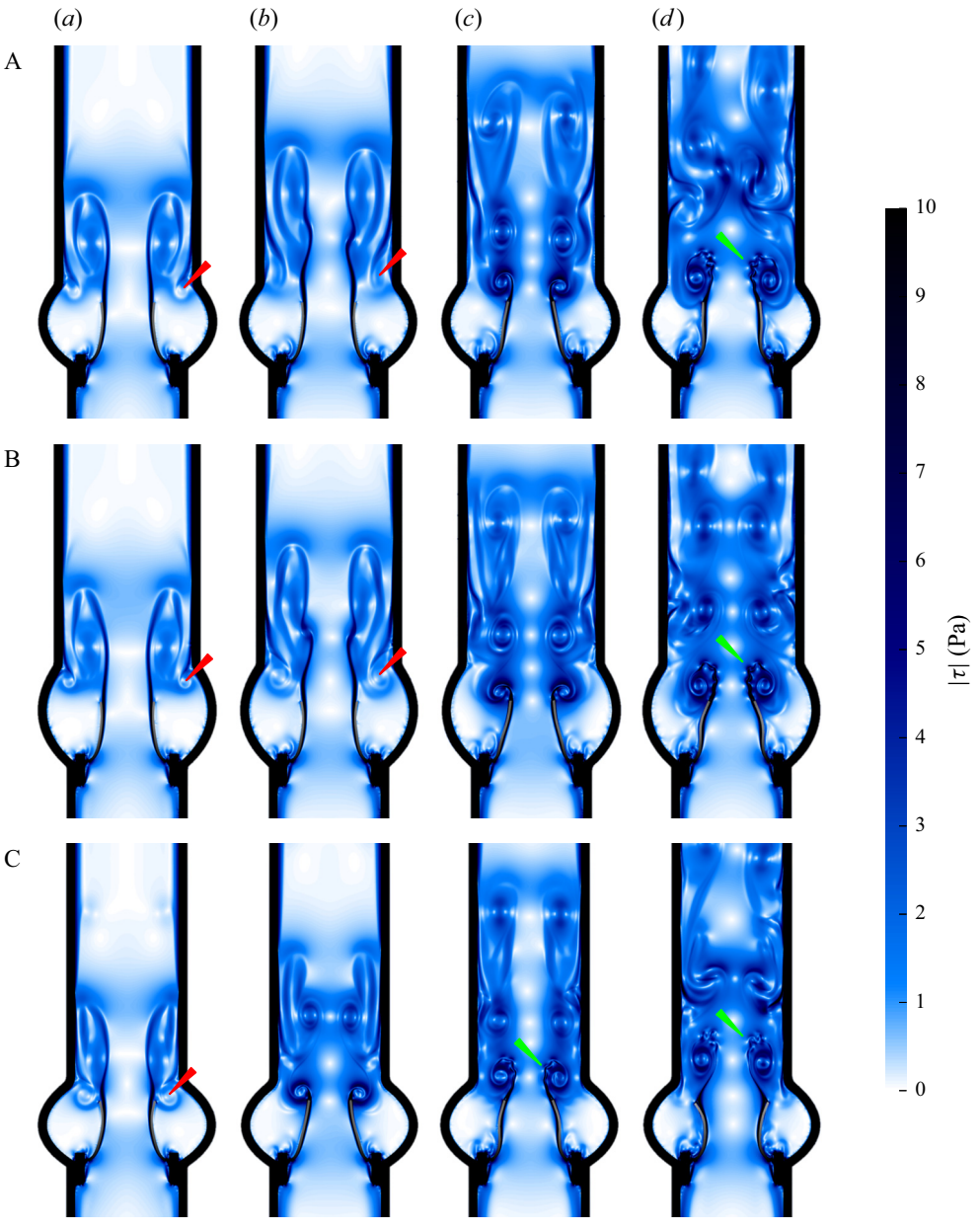

Figure 11. Instantaneous viscous shear stress magnitude $|\tau|$ for aortic wall configurations (A) initial configuration, (B) increased sinus height and (C) decreased AAo radius at (*a*) $t = 0.125$ s, (*b*) $t = 0.15$ s, (*c*) $t = 0.175$ s and (*d*) $t = 0.20$s. Secondary vortical structures forming after the impingement of the starting (primary) vortex on the aortic wall are shown by the red arrows.

Figure 13(*a*) displays the temporal evolution of transversal velocity profiles that were obtained along the leaflet shear layer downstream of the valve for case AR (rigid leaflet). In this figure, we can identify the onset and propagation of the KH instability as 'ridges'. The red line in figure 13(*a*) indicates the phase speed $c_{r,2}(\alpha_2)$ of KH instabilities according to the LSA for the configuration b_2 (free jet). There is a reasonably good agreement between

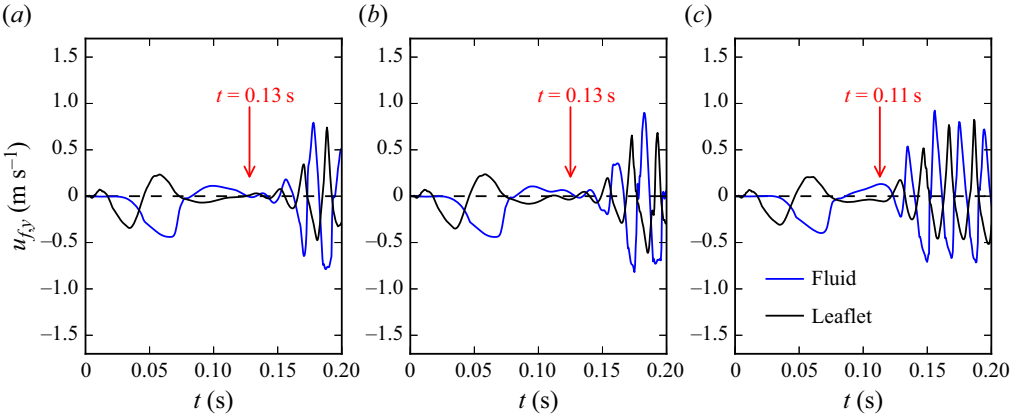

Figure 12. Temporal evolution of transversal fluid velocities extracted at $x = 6t_L$ downstream of the instantaneous leaflet tip position (blue) and transversal leaflet tip velocity (black) for aortic wall configurations (*a*) initial configuration (case A), (*b*) increased sinus height (case B) and (*c*) decreased AAo radius (case C) with the onset of transversal oscillations indicated by the red arrow.

the propagation speed of the ridges and the phase speed $c_{r,2}$ especially before $t \approx 0.17$ s when the amplitude of the instability is still small.

Figure 13(*b*) shows the transversal velocity profiles in the leaflet shear layer of case A (flexible leaflet) and the deformation of the leaflet beneath. The phase speeds $c_{r,2}(\alpha_2)$ (free jet) and $c_{r,3}(\alpha_3)$ (jet with flexible wall) are added as red lines. At the onset of the shear layer instabilities, the perturbations seem to propagate with a phase speed comparable to $c_{r,2}(\alpha_2)$. However, after the onset of leaflet motions, which appear to propagate with phase speed $c_{r,3}(\alpha_3)$, the shear layer perturbations appear to accelerate somewhat towards the phase speed $c_{r,3}(\alpha_3)$.

Furthermore, figure 13(*a*,*b*) reveals that the shear layer instability also grows in the upstream direction (indicated by thin black lines). This is reminiscent of an absolute instability (Huerre & Monkewitz 1990; Schmid & Henningson 2001) which may be facilitated by the lower streamwise velocities in the wake of the leaflet (figure 13*c*). Furthermore, this could suggest that the shear layer instability, which starts downstream of the leaflets, is triggering the FSI instability when it reaches the leaflets.

The growth rates of FSI-DNS and LSA results are compared in figure 13(*d*). Solid lines show the envelope of transversal velocity oscillations over time within the leaflet shear layer for case AR ($G_{AR}|_{x=6t_L}$) and case A ($G_A|_{x=6t_L}$) and for the leaflet tip of case A ($G_A|_{x=0}$). For comparison with growth rates obtained by LSA, we display the maximum temporal growth of KH instabilities of base flow b_2 ($\exp(\omega_{i,2,max}t)$) and of FSI instabilities of base flow b_3 ($\exp(\omega_{i,3,max}t)$). The initial growth of the shear layer instabilities in the FSI-DNS is in very good agreement with the predicted growth rate of configuration b_2 (free jet). Likewise, the growth of the leaflet instabilities agrees well with the growth rate from configuration b_3 (jet bounded by flexible wall). For better comparison, the different onsets of instability growth are marked by circles in figure 13(*a*,*b*), although the small initial amplitudes are not evident in this figure.

Finally, we study the leaflet shape in figure 13(*b*) in comparison with wavelengths determined by LSA. In the numerical simulations, the leaflet mostly exhibits an S-shaped travelling wave pattern. In LSA, this leaflet form corresponds approximately to the wavenumber $\alpha_0 = 5.55$ resulting in one full wave per leaflet length. As illustrated in figure 3, the eigenmodes at this wavenumber show a decoupled behaviour where only

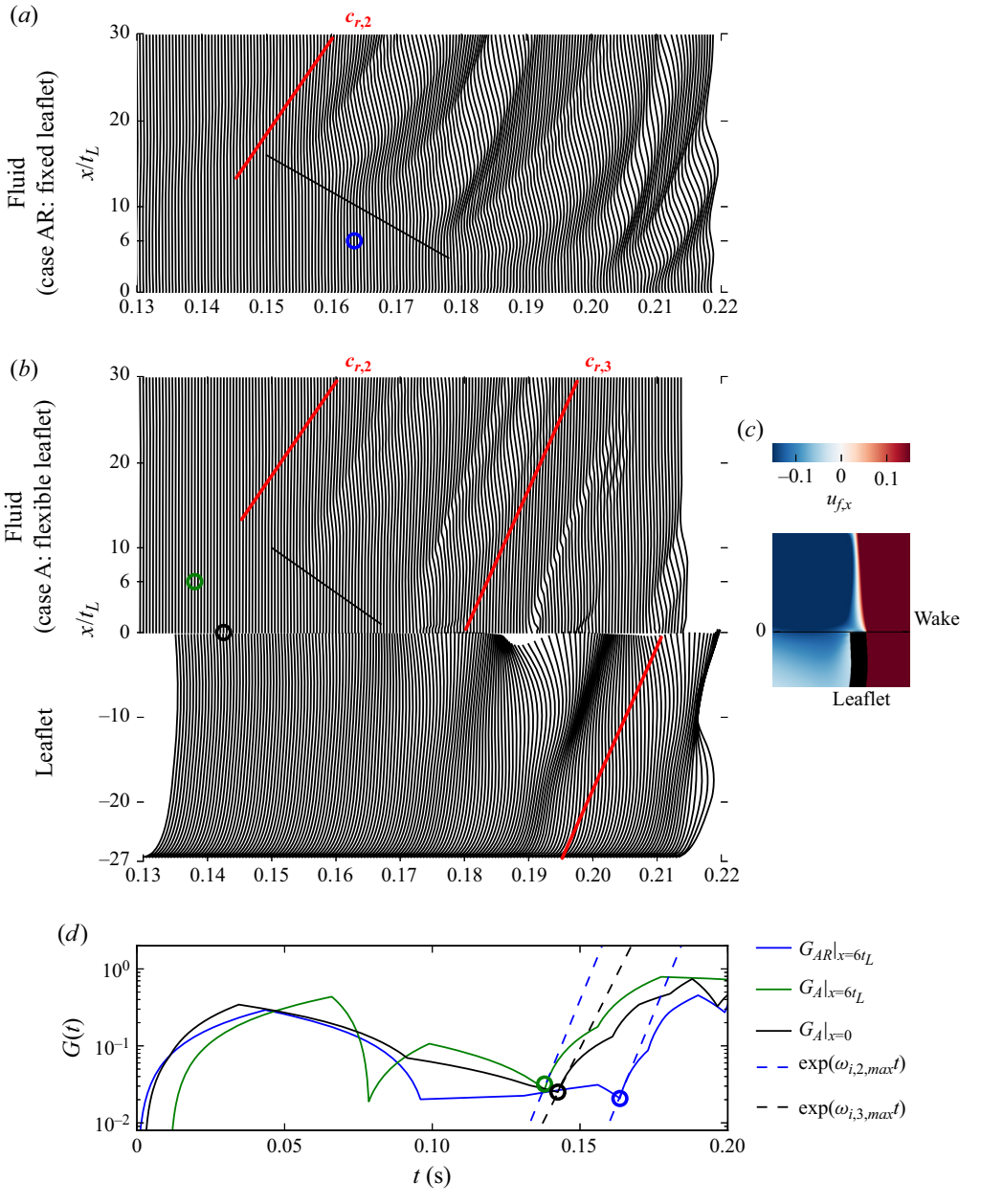

Figure 13. (*a*) Case AR: transversal velocity profiles over time along the leaflet shear layer. Red line: phase speed $c_{r,2}(\alpha_2)$ for base flow b_2 (pure shear flow). (*b*) Case A: transversal velocity profiles over time along the leaflet shear layer (top row) and leaflet shape over time (bottom row). Red line: phase speed $c_{r,3}(\alpha_3)$ for base flow b_3 (flexible wall). Black lines indicate the upstream propagation of velocity 'ridges'. (*c*) Streamwise velocity field in the leaflet wake at $t = 0.14$ s. (*d*) Envelope $G(t)$ of transversal velocity at $x = 6t_L$ for case AR ($G_{AR}|_{x=6t_L}$) and case A ($G_A|_{x=6t_L}$) and of the leaflet tip for case A ($G_A|_{x=0}$). Dashed lines show $\exp(\omega_{i,2,max}t)$ of base flow b_2 (shear flow) and $\exp(\omega_{i,3,max}t)$ of base flow b_3 (flexible wall).

one shear layer (or flexible wall) is affected by the instability, whereas the other shear layer (flexible wall) is not affected. This suggests individual, decoupled dynamics for each leaflet, which agrees well with experimental studies of leaflet kinematics which indicate asynchronous motion of the leaflets (Vennemann *et al.* 2018).

5. Conclusions

In this study, we investigated instability mechanisms which may contribute to laminar–turbulent transition downstream of a BHV. We used two conceptionally different approaches: LSA and numerical FSI simulations.

In the first part of this study (LSA) we derived modified Orr–Sommerfeld equations with an FSI extension term. We constructed a simplified one-dimensional model with a central jet and a zero-flow region surrounding the jet. The jet was confined either by a rigid wall (modelling the flow through a valve with fixed leaflets) or by a flexible wall (flow through a valve with flexible leaflets). In a third configuration, there was no wall between the jet and the zero-flow region (modelling the free aortic jet flowing into the AAo). The confined jet (fixed leaflets) was linearly stable for a physiological Reynolds number of $Re = 3318$. The configuration with a flexible wall exhibited FSI instabilities beyond a critical Reynolds number of $Re_{FSI} = 184$. For the configuration without separating wall, we found KH instabilities for a somewhat wider range of wavenumbers and a slightly higher critical Reynolds number ($Re_{KH} = 299$). At $Re = 3318$, the KH instabilities had a higher maximum growth rate and slower phase speeds than the FSI instabilities. For low wavenumbers, the unstable modes had either sinous or varicose character such that the associated displacements of the flexible walls were either in phase or out of phase, respectively. For higher wavenumbers, however, the unstable modes were decoupled such that the two flexible walls could move independently from each other.

Second, we conducted FSI simulations for a two-dimensional symmetric model of the aortic root comprising valve leaflets, a valve stent and a parametrized aortic wall model immersed in a fluid domain. To study the influence of FSI on the onset of instabilities, we ran simulations for rigid as well as flexible leaflets. Both models showed qualitatively similar flow phenomena. First, a starting vortex is formed which is advected and elongated in the downstream direction. The interaction of this starting vortex with the aortic wall leads to a secondary vortex. This vortex moves towards the leaflet shear layer and perturbs it. We suspect that this triggers the KH shear layer instability. This sequence is observed in the shear layers behind rigid and flexible leaflets which indicates that this part of the instability mechanism is independent of FSI. Only after the onset of KH instabilities do the flexible leaflets start moving with growing amplitude which results in repeated shedding of vortices from the leaflet tips. These vortices eventually break down and contribute to the chaotic nature of the fully developed flow field downstream of the valve. Simulations in a model with a narrower AAo exhibited an earlier onset of the KH instabilities. This supports the interpretation that the onset of the KH instability is triggered by the secondary vortex, because this vortex has to travel a shorter distance (in the narrow aorta case) before it reaches the shear layer. Furthermore, this indicates that the spanwise distance between aortic wall and leaflet shear layer is an important parameter for the temporal evolution of the instabilities.

The study is concluded by a combined analysis of the numerical data and the results from LSA. The results of both approaches are in good agreement. The combined analysis supports the higher growth rate of the KH instabilities in the shear layer and the higher phase speeds of FSI instabilities on the leaflets. The wavelength of the leaflet oscillations

corresponds to a modal wavenumber for which the LSA indicates decoupled eigenmodes. This could offer an explanation for the experimental observation that valve leaflets tend to move independently from each other. Additionally, the investigation of the spatio-temporal evolution of the KH instability suggests that it has the character of an absolute instability. This could mean that the onset of the leaflet oscillation (FSI instability) is triggered by the KH instability which initiates somewhat downstream of the leaflets and propagates upstream towards the leaflet.

By investigating the fundamental instability mechanisms in the flow field downstream of a BHV, our results could be useful for valve design optimization. We have shown that both KH and FSI instabilities are present at a physiologically realistic Reynolds number of $Re = 3318$. The critical Reynolds numbers for both instabilities are significantly smaller than physiological Reynolds numbers. Therefore, it is likely that transition to turbulence will occur in any aortic valve regardless of its specific design. At the same time, this means that complete suppression of transition is probably not possible. However, a better understanding of the transition mechanisms may help to find ways to modify the transition process which could contribute to improving hydraulic valve performance, increasing valve durability or reducing blood trauma. Additionally, we showed the relevance of aortic wall geometry (e.g. spanwise distance between leaflet shear layer and aortic wall) for the onset of instabilities. Therefore, patient-specific assessment of this geometrical parameter may allow for a more favourable positioning of the valve with respect to the aortic wall which could result in a delayed KH instability. This could even help to mitigate unfavourable haemodynamic mechanisms such as shear-induced thrombosis. Furthermore, optimized leaflet rigidity might dampen the FSI instability and contribute to reduced leaflet fluttering. Thereby, not only could the cyclic stresses contributing to leaflet fatigue be lowered, but also vortex shedding after the onset of oscillatory leaflet motion could be reduced which further mitigates adverse haemodynamic effects.

It is very likely that a full three-dimensional configuration of a real heart valve prosthesis features many more instability phenomena, e.g. azimuthal modes of vortex ring breakdown as present in figure 5 of Becsek *et al.* (2020). Regarding the structural side of the FSI problem, the influence of radial tension within the actual three-dimensional, curved leaflet shape might influence the leaflet motion as well as its impact on downstream flow features. Therefore, the proposed instability mechanism (starting vortex $\rightarrow$ secondary vortex at the aortic wall $\rightarrow$ KH instability in the shear layer $\rightarrow$ FSI instability on the leaflets) is only a first hypothesis and requires further investigation and confirmation.

Funding. This work was supported by a grant from the Swiss National Supercomputing Centre (CSCS) under project ID s1121.

Declaration of interests. The authors report no conflict of interest.

Author ORCIDs.
Karoline-Marie Bornemann https://orcid.org/0000-0001-7505-9283;
Dominik Obrist https://orcid.org/0000-0002-6062-9076.

Appendix A. Definition of base flows

Base flow profiles are extracted from numerical results as presented in § 3. After the initial outward leaflet deflection (opening of the valve), the leaflets remain stable for a certain time period. We define the time instance just prior to the onset of leaflet oscillations as a quasi-steady base flow solution and assume locally parallel flow. The flow profile is then extracted between the leaflet tips in the spanwise direction as shown in figure 1 (green line).

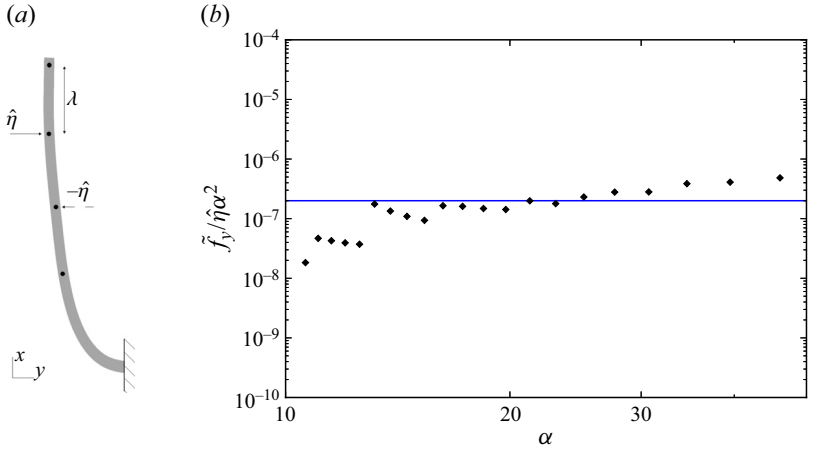

Figure 14. (*a*) Imposition of fixed value displacement amplitude $\hat{\eta}$ at varying distances λ. (*b*) Determination of material-specific spring constant ξ (blue line) by evaluating the horizontal restoring force $f_y/\hat{\eta}\alpha^2$ for different wavenumbers $\alpha = 2\pi/\lambda$.

With inflow conditions tuned to achieve a physiological cardiac output at rest, dimensional analysis of the base flow at the orifice yields a Reynolds number of $Re = 3318$.

Appendix B. Derivation of the material constant ξ

To determine the material constant ξ in the formulation of the force density $\tilde{\boldsymbol{f}}_{FSI}$, we assume proportionality of the restoring force density of the structure to the squared wavenumber α^2 (Lebbal *et al.* 2022). In order to ensure the transferability of FSI-DNS and LSA results, we conduct purely structural finite-element simulations for a single leaflet considering its thickness and neo-Hookean material model applied in numerical simulations. As shown in figure 14, a defined displacement amplitude $\hat{\eta}$ at varying wavelengths λ is imposed from alternating sides to map the restoring force resulting in a non-dimensionalized material-specific constant of $\xi = 2 \times 10^{-7}$.

Appendix C. Sensitivity analysis

Figure 15 summarizes the sensitivity of the LSA and the numerical FSI simulations to variations in element size. Maximum growth rates $\omega_{i,max}$ converge at 400 grid points for both b_2 and b_3 base flows. Sensitivity analysis regarding the fluid mesh width of the FSI simulations was conducted for minimal mesh widths of 35, 70 and 140 µm. Results were compared at the STJ and within the leaflet shear layer at a critical time $t = 0.13$ s which marks the onset of transversal fluid oscillations. Also, the temporal evolution of leaflet tip displacements was assessed to investigate the sensitivity of structural motion to fluid mesh widths. In general, a fluid mesh width of 70 µm is found to be sufficient for converged results. However, better numerical performance (i.e. fewer spurious oscillations at the FSI, more stable numerical convergence) is reached for smaller mesh widths. Therefore, a minimum mesh width of 35 µm was used for this study. For this mesh width, a maximum time step of 1 µs is necessary to achieve numerical stability.

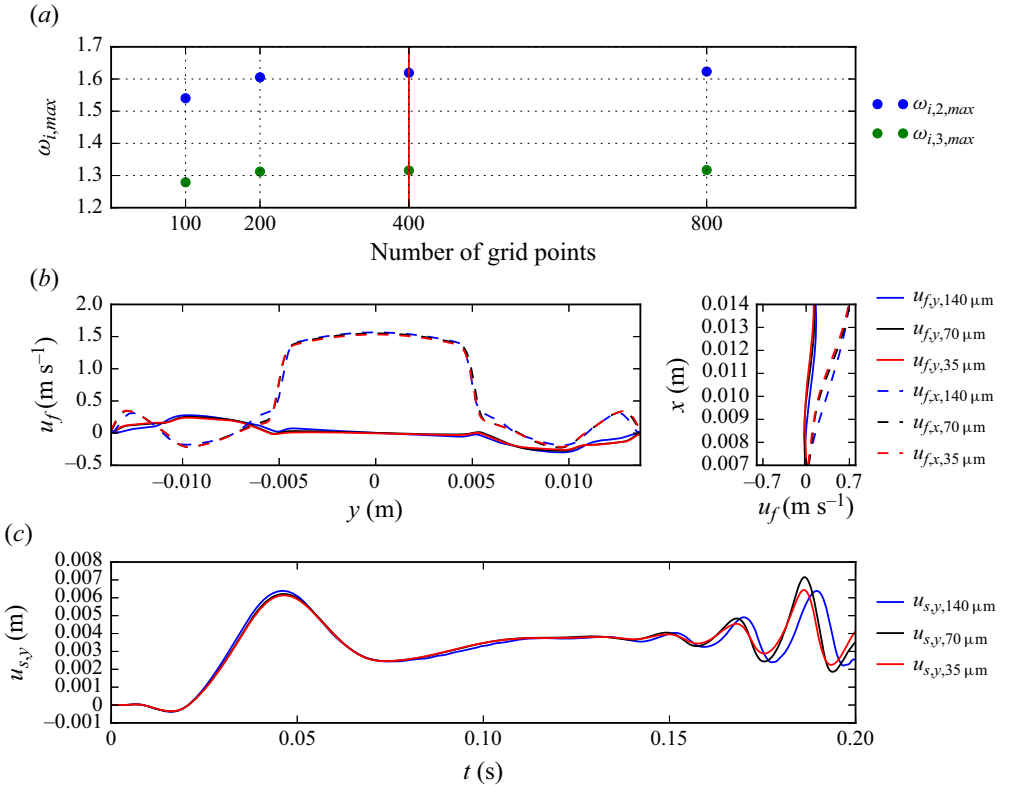

Figure 15. Sensitivity analysis of LSA: (*a*) maximum growth rate $\omega_{i,max}$ for base flows b_2 (shear flow, blue) and b_3 (flexible wall, green). A number of grid points of 400 (indicated by the red line) was chosen for this study. Sensitivity analysis of numerical FSI simulations: (*b*) transversal ($u_{f,y}$) and streamwise ($u_{f,x}$) velocity profiles at the STJ (left) and within the leaflet shear layer (right) for minimal fluid mesh widths 35, 70 and 140 µm at time instant $t = 0.13$ s; (*c*) temporal evolution of the leaflet tip displacement $u_{s,y}$ for minimal fluid mesh widths 35, 70 and 140 µm.

References

Asadi, H. & Borazjani, I. 2023 A contact model based on the coefficient of restitution for simulations of bio-prosthetic heart valves. *Intl J. Numer. Meth. Biomed. Engng* **39** (9), e3754.

Bahlmann, E., Nienaber, C.A., Cramariuc, D., Gohlke-Baerwolf, C., Ray, S., Devereux, R.B., Wachtell, K., Kuck, K.H., Davidsen, E. & Gerdts, E. 2011 Aortic root geometry in aortic stenosis patients (a SEAS substudy). *Eur. J. Echocardiogr.* **12** (8), 585–590.

Bavo, A.M., Rocatello, G., Iannaccone, F., Degroote, J., Vierendeels, J. & Segers, P. 2016 Fluid-structure interaction simulation of prosthetic aortic valves: comparison between immersed boundary and arbitrary Lagrangian–Eulerian techniques for the mesh representation. *PLoS ONE* **11** (4), e0154517.

Becsek, B., Pietrasanta, L. & Obrist, D. 2020 Turbulent systolic flow downstream of a bioprosthetic aortic valve: velocity spectra, wall shear stresses, and turbulent dissipation rates. *Front. Physiol.* **11**, 1–19.

Boraita, A., Heras, M.E., Morales, F., Marina-Breysse, M., Canda, A., Rabadan, M., Barriopedro, M.I., Varela, A., De La Rosa, A. & Tuñón, J. 2016 Reference values of aortic root in male and female white elite athletes according to sport. *Circulation* **9** (10), 1–10.

Borazjani, I. 2013 Fluid-structure interaction, immersed boundary-finite element method simulations of bio-prosthetic heart valves. *Comput. Meth. Appl. Mech. Engng* **257**, 103–116.

Buellesfeld, L., *et al.* 2013 Aortic root dimensions among patients with severe aortic stenosis undergoing transcatheter aortic valve replacement. *JACC Cardiovasc. Interv.* **6** (1), 72–83.

Chandra, S., Rajamannan, N.M. & Sucosky, P. 2012 Computational assessment of bicuspid aortic valve wall-shear stress: implications for calcific aortic valve disease. *Biomech. Model. Mechanobiol.* **11** (7), 1085–1096.

CHEN, Y. & LUO, H. 2018 A computational study of the three-dimensional fluid–structure interaction of aortic valve. *J. Fluids Struct.* **80**, 332–349.

CHEN, Y. & LUO, H. 2020 Pressure distribution over the leaflets and effect of bending stiffness on fluid-structure interaction of the aortic valve. *J. Fluid Mech.* **883**, A52.

DE HART, J., PETERS, G.W.M., SCHREURS, P.J.G. & BAAIJENS, F.P.T. 2000 A two-dimensional fluid-structure interaction model of the aortic value. *J. Biomech.* **33** (9), 1079–1088.

DVIR, D., *et al*. 2018 Standardized definition of structural valve degeneration for surgical and transcatheter bioprosthetic aortic valves. *Circulation* **137** (4), 388–399.

EGBE, A.C., PISLARU, S.V., PELLIKKA, P.A., POTERUCHA, J.T., SCHAFF, H.V., MALESZEWSKI, J.J. & CONNOLLY, H.M. 2015 Bioprosthetic valve thrombosis versus structural failure. *J. Am. Coll. Cardiol.* **66** (21), 2285–2294.

GALLO, D., MORBIDUCCI, U. & DE TULLIO, M.D. 2022 On the unexplored relationship between kinetic energy and helicity in prosthetic heart valves hemodynamics. *Intl J. Engng Sci.* **177**, 103702.

GILMANOV, A., STOLARSKI, H. & SOTIROPOULOS, F. 2018 Flow–structure interaction simulations of the aortic heart valve at physiologic conditions: the role of tissue constitutive model. *J. Biomech. Engng* **140** (4), 041003.

GOMEL, M.A., LEE, R. & GRANDE-ALLEN, K.J. 2019 Comparing the role of mechanical forces in vascular and valvular calcification progression. *Front. Cardiovasc. Med.* **5**, 1–14.

HAJ-ALI, R., MAROM, G., BEN ZEKRY, S., ROSENFELD, M. & RAANANI, E. 2012 A general three-dimensional parametric geometry of the native aortic valve and root for biomechanical modeling. *J. Biomech.* **45** (14), 2392–2397.

HASLER, D. & OBRIST, D. 2018 Three-dimensional flow structures past a bioprosthetic valve in an in-vitro model of the aortic root. *PLoS ONE* **13** (3), e0194384.

HATOUM, H., YOUSEFI, A., LILLY, S., MAUREIRA, P., CRESTANELLO, J. & DASI, L.P. 2018 An in vitro evaluation of turbulence after transcatheter aortic valve implantation. *J. Thorac. Cardiov. Sur.* **156** (5), 1837–1848.

HEAD, S.J., ÇELIK, M. & KAPPETEIN, A.P. 2017 Mechanical versus bioprosthetic aortic valve replacement. *Eur. Heart J.* **38** (28), 2183–2191.

HEDAYAT, M., ASGHARZADEH, H. & BORAZJANI, I. 2017 Platelet activation of mechanical versus bioprosthetic heart valves during systole. *J. Biomech.* **56**, 111–116.

HENNIGER, R., OBRIST, D. & KLEISER, L. 2010 High-order accurate solution of the incompressible Navier–Stokes equations on massively parallel computers. *J. Comput. Phys.* **229** (10), 3543–3572.

HIROMI SPÜHLER, J. & HOFFMAN, J. 2020 An interface-tracking unified continuum model for fluid-structure interaction with topology change and full-friction contact with application to aortic valves. *Intl J. Numer. Meth. Engng* **2020**, 5258–5278.

HOLMES, D.R. & MACK, M.J. 2017 Aortic valve bioprostheses: leaflet immobility and valve thrombosis. *Circulation* **135** (18), 1749–1756.

HOLZAPFEL, G.A., GASSER, T.C. & OGDEN, R.W. 2000 A new constitutive framework for arterial wall mechanics and a comparative study of material models. *J. Elast.* **61** (1–3), 1–48.

HUERRE, P. & MONKEWITZ, P.A. 1990 Local and global instabilities in spatially developing flows. *Annu. Rev. Fluid Mech.* **22**, 473–537.

JAHREN, S.E., HEINISCH, P.P., HASLER, D., WINKLER, B.M., STORTECKY, S., PILGRIM, T., LONDONO, M.C., CARREL, T., VON TENGG-KOBLIGK, H. & OBRIST, D. 2018 Can bioprosthetic valve thrombosis be promoted by aortic root morphology. An in vitro study? *Interact. Cardiovasc. Thorac. Surg.* **27** (1), 108–115.

JOHNSON, E.L., RAJANNA, M.R., YANG, C.H. & HSU, M.C. 2022 Effects of membrane and flexural stiffnesses on aortic valve dynamics: identifying the mechanics of leaflet flutter in thinner biological tissues. *Forces Mech.* **6**, 100053.

JOHNSON, E.L., WU, M.C.H., XU, F., WIESE, N.M., RAJANNA, M.R., HERREMA, A.J., GANAPATHYSUBRAMANIAN, B., HUGHES, T.J.R., SACKS, M.S. & HSU, M.-C. 2020 Thinner biological tissues induce leaflet flutter in aortic heart valve replacements. *Proc. Natl Acad. Sci. USA* **117** (32), 19007–19016.

KHERADVAR, A., *et al*. 2015 Emerging trends in heart valve engineering. Part 2. Novel and standard technologies for aortic valve replacement. *Ann. Biomed. Engng* **43** (4), 844–857.

KLUSAK, E. & QUINLAN, N.J. 2019 High-resolution measurements of leakage flow inside the hinge of a large-scale bileaflet mechanical heart valve hinge model. *Cardiovasc. Engng Technol.* **10** (3), 469–481.

LEBBAL, S., ALIZARD, F. & PIER, B. 2022 Revisiting the linear instabilities of plane channel flow between compliant walls. *Phys. Rev. Fluids* **7** (2), 1–32.

LEE, J.H., RYGG, A.D., KOLAHDOUZ, E.M., ROSSI, S., RETTA, S.M., DURAISWAMY, N., SCOTTEN, L.N., CRAVEN, B.A. & GRIFFITH, B.E. 2020 Fluid–structure interaction models of bioprosthetic heart valve dynamics in an experimental pulse duplicator. *Ann. Biomed. Engng* **48** (5), 1475–1490.

LEE, J.H., SCOTTEN, L.N., HUNT, R., CARANASOS, T.G., VAVALLE, J.P. & GRIFFITH, B.E. 2021 Bioprosthetic aortic valve diameter and thickness are directly related to leaflet fluttering: results from a combined experimental and computational modeling study. *JTCVS Open* **6**, 60–81.

LI, K.Y.C. 2019 Bioprosthetic heart valves: upgrading a 50-year old technology. *Front. Cardiovasc. Med.* **6**, 1–6.

MIREA, O., MAFFESSANTI, F., GRIPARI, P., TAMBORINI, G., MURATORI, M., FUSINI, L., CLAUDIA, C., FIORENTINI, C., PLESEA, I.E. & PEPI, M. 2013 Effects of aging and body size on proximal and ascending aorta and aortic arch: inner edge-to-inner edge reference values in a large adult population by two-dimensional transthoracic echocardiography. *J. Am. Soc. Echocardiogr.* **26** (4), 419–427.

NESTOLA, M.G.C., BECSEK, B., ZOLFAGHARI, H., ZULIAN, P., DE MARINIS, D., KRAUSE, R. & OBRIST, D. 2019 An immersed boundary method for fluid-structure interaction based on variational transfer. *J. Comput. Phys.* **398**, 108884.

NORDSTRÖM, J., NORDIN, N. & HENNINGSON, D. 1999 Fringe region technique and the Fourier method used in the direct numerical simulation of spatially evolving viscous flows. *SIAM J. Sci. Comput.* **20** (4), 1365–1393.

OECHTERING, T.H., *et al*. 2019 In vitro 4D flow MRI evaluation of aortic valve replacements reveals disturbed flow distal to biological but not to mechanical valves. *J. Card. Surg.* **34** (12), 1452–1457.

ORLANDI, P. & VERZICCO, R. 1993 Vortex rings impinging on walls: axisyrnmetric and three-dimensional simulations. *J. Fluid Mech.* **256**, 615–646.

PESKIN, C.S. 2002 The immersed boundary method. *Acta Numerica* **11**, 479–517.

PURI, R., AUFFRET, V. & RODÉS-CABAU, J. 2017 Bioprosthetic valve thrombosis. *J. Am. Coll. Cardiol.* **69** (17), 2193–2211.

REUL, H., VAHLBRUCH, A., GIERSIEPEN, M., SCHMITZ-RODE, T., HIRTZ, V. & EFFERT, S. 1990 Technical note the geometry of the aortic root in health. *J. Biomech.* **23** (2), 181–191.

SAIKRISHNAN, N., YAP, C.H., MILLIGAN, N.C., VASILYEV, N.V. & YOGANATHAN, A.P. 2012 In vitro characterization of bicuspid aortic valve hemodynamics using particle image velocimetry. *Ann. Biomed. Engng* **40** (8), 1760–1775.

SCHMID, P.J. & HENNINGSON, D.S. 2001 *Stability and Transition in Shear Flows*, Applied Mathematical Sciences, vol. 142. Springer.

SOARES, J.S., FEAVER, K.R., ZHANG, W., KAMENSKY, D., AGGARWAL, A. & SACKS, M.S. 2016 Biomechanical behaviour of bioprosthetic heart valve heterograft tissues: characterization, simulation, and performance. *Cardiovasc. Engng Technol.* **7** (4), 309–351.

TISSEUR, F. 2000 Backward error and condition of polynomial eigenvalue problems. *Linear Algebra Appl.* **309**, 339–361.

TSOLAKI, E., *et al*. 2023 Multiscale multimodal characterization and simulation of structural alterations in failed bioprosthetic heart valves. *Acta Biomaterialia* **169**, 138–154.

DE TULLIO, M.D. & PASCAZIO, G. 2016 A moving-least-squares immersed boundary method for simulating the fluid–structure interaction of elastic bodies with arbitrary thickness. *J. Comput. Phys.* **325**, 201–225.

VENNEMANN, B., RÖSGEN, T., HEINISCH, P.P. & OBRIST, D. 2018 Leaflet kinematics of mechanical and bioprosthetic aortic valve prostheses. *ASAIO J.* **64** (5), 651–661.

VRIZ, O., *et al*. 2014 Normal values of aortic root dimensions in healthy adults. *Am. J. Cardiol.* **114** (6), 921–927.

WALKER, J.D.A., SMITH, C.R., CERRA, A.W. & DOLIGALSKI, T.L. 1987 The impact of a vortex ring on a wall. *J. Fluid Mech.* **181**, 99–140.

YOGANATHAN, A.P., HE, Z. & JONES, S.C. 2004 Fluid mechanics of heart valves. *Annu. Rev. Biomed. Engng* **6**, 331–362.

YUN, B.M., DASI, L.P., AIDUN, C.K. & YOGANATHAN, A.P. 2014 Computational modelling of flow through prosthetic heart valves using the entropic lattice-Boltzmann method. *J. Fluid Mech.* **743**, 170–201.

ZOLFAGHARI, H., KERSWELL, R.R., OBRIST, D. & SCHMID, P.J. 2022 Sensitivity and downstream influence of the impinging leading-edge vortex instability in a bileaflet mechanical heart valve. *J. Fluid Mech.* **936**, A41.

ZOLFAGHARI, H. & OBRIST, D. 2019 Absolute instability of impinging leading edge vortices in a submodel of a bileaflet mechanical heart valve. *Phys. Rev. Fluids* **4** (12), 123901.

ZOLFAGHARI, H. & OBRIST, D. 2021 A high-throughput hybrid task and data parallel Poisson solver for large-scale simulations of incompressible turbulent flows on distributed GPUs. *J. Comput. Phys.* **437**, 110329.